

Conceptual study of energy resolved x-ray measurement and electron temperature reconstruction on ITER with low voltage ionization chambers

Cite as: Rev. Sci. Instrum. 92, 083511 (2021); doi: 10.1063/5.0028460

Submitted: 4 September 2020 • Accepted: 14 June 2021 •

Published Online: 10 August 2021



View Online



Export Citation



CrossMark

D. Colette,^{1,a)}  D. Mazon,¹ R. Barnsley,² M. O'Mullane,³  A. Jardin,⁴  and A. Sirinelli²

AFFILIATIONS

¹CEA, IRFM, F-13108 Saint Paul Lez Durance, France

²ITER Organization, Route de Vinon sur Verdon, 13067 St Paul Lez Durance Cedex, France

³Department of Physics SUPA, University of Strathclyde, Glasgow G4 0NG, United Kingdom

⁴Institute of Nuclear Physics Polish Academy of Sciences (IFJ PAN), PL-31-342 Krakow, Poland

^{a)} Author to whom correspondence should be addressed: damien.colette@iter.org

ABSTRACT

In tokamaks with tungsten-based plasma facing components, such as ITER, pollution of the plasma by heavy impurities is a major concern as it can lead to radiative breakdown. The radiation emitted by such impurities is mainly composed of x-rays in the [0.1; 100] keV range. A diagnostic allowing for the reconstruction of the impurity distribution is of high interest. The ITER requirements for the x-ray measurement system make it mandatory for the detector to provide spectral information. Due to the radiation environment during the ITER nuclear phase, advanced detectors exhibiting high resilience to neutrons and *gamma* rays, such as gas-filled detectors, are required. The use of Low Voltage Ionization Chambers (LVICs) for this purpose is investigated in this paper. Several anodes have been added to the detector in order to allow for spectral deconvolution. This article presents a conceptual study of the use of a multi-anode LVIC for energy resolved x-ray measurement on ITER. It covers the design of the multi-anode LVIC and its modeling, the method for spectral deconvolution, and its application to energy resolved x-ray tomography, as well as the computation of the electron temperature from the reconstructed local x-ray emissivity.

Published under an exclusive license by AIP Publishing. <https://doi.org/10.1063/5.0028460>

I. INTRODUCTION

With the advent of tungsten (W) as the main candidate for the plasma-facing components of ITER and future fusion reactors, impurity accumulation has become a key challenge for fusion research.¹ Due to its high atomic number, W can radiate a very large amount of power out of the plasma and therefore decrease the reactor performance.² In current tokamaks equipped with W, the emitted radiation is mostly located in the soft x-ray (SXR) range ($h\nu < 20$ keV).³ Therefore, SXR radiation mainly depends on impurity densities, and SXR tomography allows for the reconstruction of local impurity density profiles.⁴

The emitted x-ray spectrum is composed of a continuum on top of which discrete lines are added. The lines result from line radiation and are located at low energy ($h\nu < 20$ keV), and the continuum

results from both electron bremsstrahlung and radiative recombination. In high power plasmas, such as ITER and DEMO, and even in the absence of suprathermal electrons, the high electron temperature leads to a high energy x-ray continuum: a non-negligible signal can be observed up to 100 keV.⁵ The continuum emissivity spectrum follows an exponential curve, with a slope that is proportional to $h\nu/T_e$. Therefore, energy deconvolution of the x-ray spectrum in an energy range where bremsstrahlung is dominant allows for the estimation of the local electron temperature.

The ITER x-ray detector is stated as a supplementary diagnostic (which is defined as “diagnostic validates or calibrates the measurement, but is not complete in itself”) for the electron temperature and a back-up diagnostic (defined as “diagnostic providing similar data to the primary diagnostics, but has some limitations”) for the fractional content of impurities with $Z > 10$.⁶ As a result, it is

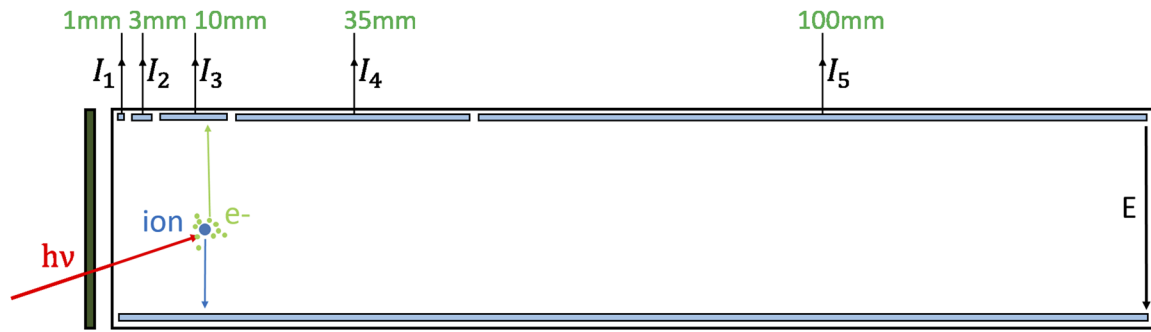


FIG. 1. Schematic representation of a multi-anode LVIC with five anodes of respective sizes: 1, 3, 10, 35, and 100 mm. These anode sizes are used with 5 bars of argon for spectral deconvolution in Sec. V B. The width of the chamber has been enlarged for visualization purposes and will be of around 2 mm per channel on ITER.

mandatory for the x-ray detector to provide spectral information from the region where line radiation is dominant ($2 \text{ keV} < h\nu < 10 \text{ keV}$) to the continuum-dominated region ($10 \text{ keV} < h\nu < 100 \text{ keV}$).

Due to the high amount of neutron, gamma, and hard x-ray radiation generated in ITER during the Deuterium–Deuterium (D–D) and Deuterium–Tritium (D–T) phases, radiation resilience is a major concern for diagnostics. In the case of x-ray measurement, advanced gas detectors, such as Low Voltage Ionization Chambers (LVICs)⁷ or Gas Electron Multipliers (GEMs),⁸ are currently foreseen to remedy this situation.

Thanks to its simple design and low voltage operation, the LVIC benefits from a very high resilience to neutron, *gamma*, and hard x-ray radiation. The cost of this resilience is that the LVIC operates only in the current mode and cannot *a priori* measure the incoming photon spectrum. Nevertheless, adding anodes to the LVIC could allow spectral deconvolution to be performed on the currents measured by each chamber and therefore lead to incoming spectrum estimation.⁹

This paper investigates the use of multi-anode LVICs (see Fig. 1) for the energy resolved x-ray measurement on ITER. This study is performed through simulation of detection using a LVIC synthetic diagnostic tool in the real ITER geometry coupled to an original energy deconvolution algorithm. Tomography is performed from these energy resolved spectra in order to reconstruct the local x-ray emissivity. The slope of the local emissivity at high energy is computed and allows for the reconstruction of the electron temperature profile. The influence of the gas filling the detection volume is studied through the comparison of argon and xenon.

In Sec. II, the LVIC proposed design is presented for ITER configuration. In Sec. III, a numerical model of the LVIC is envisaged and x-rays on ITER (emissivity and detector geometry) are described. Section IV covers the description of the method used for spectrum deconvolution. Deconvolved spectra using argon and xenon LVICs are shown in Sec. V. In Sec. VI, energy resolved tomography is performed from the results of spectrum deconvolution using xenon. The electron temperature is derived from the local emissivity spectra in Sec. VII. Finally, conclusion and perspectives are given in Sec. IX.

This paper aims at presenting the overall results of this work in a succinct way, and more exhaustive results can be found in Ref. 10.

II. LOW VOLTAGE IONIZATION CHAMBER

LVICs are gas-filled particle detectors that convert the incident radiation (x-rays in our case) into electron–ion pairs by photoionization of the gas. The generated electron cloud (respectively, ion) drifts toward the anode (respectively, cathode), thanks to the application of an electric field to the chamber. An electrical current results from this process and can be measured. The LVIC therefore operates in the current mode, which does not allow for the extraction of any spectral information.

In order to remedy this problem, an innovative multi-anode LVIC (see Fig. 1) is proposed in this paper to deconvolute the spectrum. The chamber can be divided into sub-chambers, which consist of the volume between each anode and the cathode. In this paper, we will number the sub-chambers as they are encountered by the photons while progressing inside the detection volume: the first sub-chamber will be the first volume of gas penetrated by the x-ray flux, and so on. The spectral response of the i -th subchamber is therefore expressed as

$$\eta_i(h\nu) = T(h\nu) \cdot A_i(h\nu) \cdot \prod_{k=1}^{i-1} (1 - A_k(h\nu)), \quad (1)$$

where $h\nu$ is the photon energy, T is the coefficient of transmission through the filter, and A_i is the coefficient of absorption in the i -th subchamber. The A and T coefficients are defined in Secs. III A 2 and III A 3, respectively.

The spectral response calculated from Eq. (4) in Sec. III A 3 and Eq. (3) in Sec. III A 2 is displayed in Fig. 2. The first sub-chamber tends to absorb most of the low energy photons, which leads to a near zero probability of detection of these photons in the latter sub-chambers (see Fig. 2). For high energy photons due to lower photoionization cross sections, a very small proportion of the incoming spectrum is absorbed and therefore the detection probability mainly depends on the length of the detection volume. As a result, multi-anode LVICs with increasing length of sub-chambers present a spectral response that is shifted toward higher energies from one sub-chamber to the next, as shown in Fig. 2.

Thanks to the different spectral response of each sub-chamber, the currents collected by each anode can be used to deconvolute the photon spectrum. In these conditions, spectral deconvolution is an

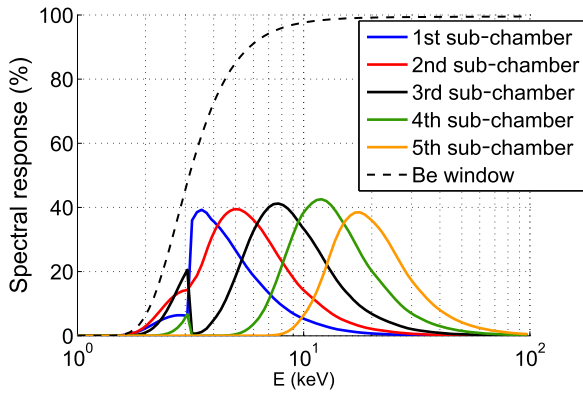


FIG. 2. Spectral response for an argon-filled LVIC with five anodes. The lengths of the sub-chambers are 1, 3, 10, 35, and 100 mm, respectively, and the filter consists of 200 μm of beryllium. The gas pressure is 5 bars.

ill-posed inversion problem. The method used for its resolution is described in Sec. IV.

III. SIMULATION OF THE DETECTION

This section covers all the aspects of simulating x-ray detection on ITER using LVIC: modeling of the detector, tokamak and lines-of-sight geometries, and emissivity scenario.

A. LVIC synthetic diagnostic

A synthetic diagnostic for gas electron multipliers⁴ has been modified in order to simulate x-ray detection using LVIC. This modeling tool computes the incoming photon flux on the detector (based on a given ITER radiative scenario), transmission through the beryllium window, photoionization of the gas, and charge collection (in the different sub-chambers). This section gives a brief description of these different modules, but a more detailed one can be found in Ref. 11.

1. Aperture-detector system

In order to significantly simplify the estimation of the photon flux impacting the detector while retaining a good accuracy, standard simplifications for tomography have been used.¹² Two approximations are used:

- The *line-of-sight (LoS) approximation*: if the radius of the cone of detection of the system is small compared to the spatial variation of the x-ray emissivity, the detection volume can be approximated by a line. The incident photon flux becomes the line integral of the emissivity multiplied by the so-called etendue of the system.
- The *pinhole approximation*: if the dimensions of the aperture are small compared to those of the detector, the etendue of the system is conserved along the line-of-sight.

With these simplifications, the photon flux impacting the detector (in $\text{ph} \cdot \text{s}^{-1}$) is given by

$$\phi = E \cdot \int_r \varepsilon(r) \cdot dr = \frac{S_A \cdot S_D}{4\pi \cdot L^2} \cdot \int_r \varepsilon(r) \cdot dr, \quad (2)$$

where E is the etendue of the system, ε is the plasma emissivity, S_A and S_D are the surface of the aperture and detector, respectively, and L is the distance between the aperture and the detector.

2. Transmission through the beryllium window

A beryllium window is used as an interface between the pressurized gas and the vacuum of the port plug on the front side of the detector. The transmission coefficients for beryllium have been calculated using cross sections from the theoretical NIST XCOM database.¹³ For a given photon energy $h\nu$, the transmission coefficient is given by

$$T(h\nu) = \exp(-d_m \cdot \sigma_{tot}(h\nu) \cdot l \cdot 10^{-28}), \quad (3)$$

where d_m is the density of the material in $\text{atom} \cdot \text{m}^{-3}$, $\sigma_{tot}(h\nu)$ is the total cross section at energy $h\nu$ in $\text{b} \cdot \text{atom}^{-1}$, and l is the width of the filter in m .

3. Gas photoionization

Photoionization of a gas is a physical process during which a photon is absorbed by an atom of gas, releasing an electron of energy $E \approx h\nu - E_b$, where $h\nu$ is the photon energy and E_b is the binding energy of the electron to the atom of the gas.

The residual energy E_b of the ion in the excited state can be released through different processes. This modeling tool used in this study simulates the dominant processes, namely, Auger emission and x-ray fluorescence. Auger emission consists of the emission of an additional electron of energy E_b . X-ray fluorescence can happen when the photon has a high enough energy to ionize an inner shell electron. It consists of the emission of an x-ray photon, which has a high probability of escaping the detection volume.

At present, two gases can be simulated by the synthetic diagnostic: argon and xenon. Argon K fluorescence takes place for $h\nu > 3.2$ keV with a probability of 14%. The energy of the emitted photon is 2.9 keV.¹⁴ Xenon K fluorescence takes place for $h\nu > 34.5$ keV with a probability of 88.9%.¹⁵ The energy of the emitted photon is 29.46 keV.

By collisioning with other atoms in the gas, the initial electron of energy $E \approx h\nu - E_b$ generates a cloud of primary electrons of population $N \approx \frac{E}{W_{eff}}$, where W_{eff} is the mean ionization energy of the gas. The population of the primary electron cloud is subject to a statistical fluctuation σ_N^2 given by $\frac{\sigma_N^2}{N^2} = \frac{F}{N}$, where F is the so-called Fano factor.¹⁶ The mean ionization energy was taken as 26 eV for argon¹⁷ and 21 eV for xenon.¹⁸ The Fano factor was taken as 0.23 for argon¹⁹ and as 0.29 for xenon.²⁰

Photoionization cross sections for both gases have been extracted from the NIST XCOM database,¹³ given in barns per atom ($\text{b} \cdot \text{atom}^{-1}$), and used to compute the probability of photoionization $A(h\nu)$ given by

$$A(h\nu) = 1 - \exp(-d_g \cdot \sigma_{ph}(h\nu) \cdot l \cdot 10^{-28}), \quad (4)$$

where d_g is the density of the gas in $\text{atom} \cdot \text{m}^{-3}$, $\sigma_{ph}(h\nu)$ is the photoionization cross section at energy $h\nu$ in $\text{b} \cdot \text{atom}^{-1}$, and l is the length of the ionization chamber in m .

4. Charge collection

The charge collection module calculates the number of electrons forming the detection signal. It relies on two simplifying assumptions on the voltage applied to the detector. Indeed, this model assumes that the electric field in the detection volume is high enough so that all the charge is collected on the electrodes (electron absorption and ion neutralization can be neglected) and so that the effect of screening of the electrodes by the transiting charge is negligible (the electric field does not vary with the incoming photon flux).

B. ITER x-ray geometry

On ITER, 12 radial x-ray cameras of 16 channels each are considered for a total of 192 lines-of-sight (radial lines in Fig. 3), each channel corresponding to a line-of-sight. In this paper, the term camera denotes the physical detector, which is divided into several channels. The term pixel is strictly reserved to the geometrical pixels of the poloidal section and is used for tomography.

It has been demonstrated in Ref. 11 that the lack of line-of-sight overlapping in this configuration does not allow for accurate tomographic reconstruction of poloidally asymmetric emissivity profiles. 60 additional lines-of-sight located in an upper port plug have been proposed (“vertical” lines in Fig. 3). The configuration containing both sets of detectors will be considered in this study.

The etendue as calculated from Eq. (2) for each detector channel is displayed in Fig. 4. For all channels, the surfaces of the detector and of the aperture are the same. Therefore, the differences observed in Fig. 4 only result from different aperture-detector distances. It can be noticed that this distance is significantly higher for the “vertical” lines-of-sight, leading to a much lower etendue.

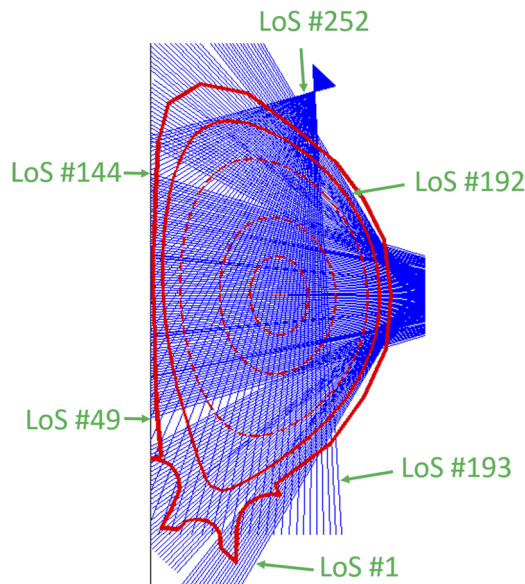


FIG. 3. Considered line-of-sight geometry of x-ray detectors in ITER. Adapted from Colette *et al.*, “Modeling a low voltage ionization chamber based tomography system on ITER,” *Rev. Sci. Instrum.* **91**, 073504 (2020) with the permission of AIP Publishing.

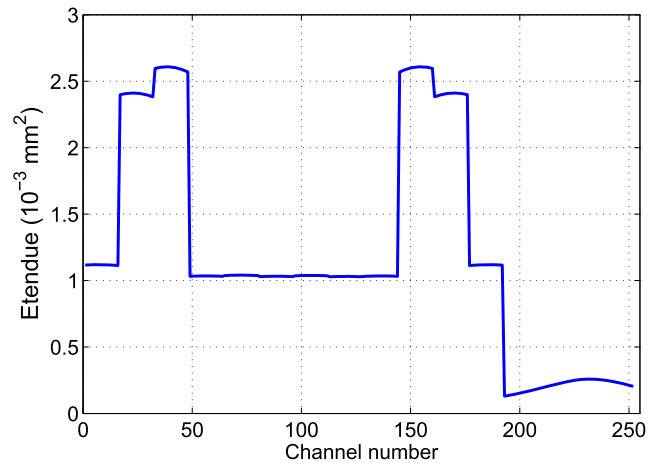


FIG. 4. Etendue of the different x-ray cameras. Radial lines-of-sight are numbered from 1 to 192 in ascending order from the bottom to the top of the vacuum vessel. “Vertical” lines-of-sight are numbered from 193 to 252 in ascending order from the low field side to the high field side. Reproduced from Colette *et al.*, “Modeling a low voltage ionization chamber based tomography system on ITER,” *Rev. Sci. Instrum.* **91**, 073504 (2020) with the permission of AIP Publishing.

C. ITER standard high power scenario

Plasma emissivity has been estimated in the context of a standard high power D-T plasma scenario.⁵ X-ray emission in the [0.001; 100] keV energy range was simulated for an impurity content of 10^{-2} of beryllium, $5 \cdot 10^{-4}$ of iron, and 10^{-5} of tungsten. The impurity density profiles are homothetic to the electron

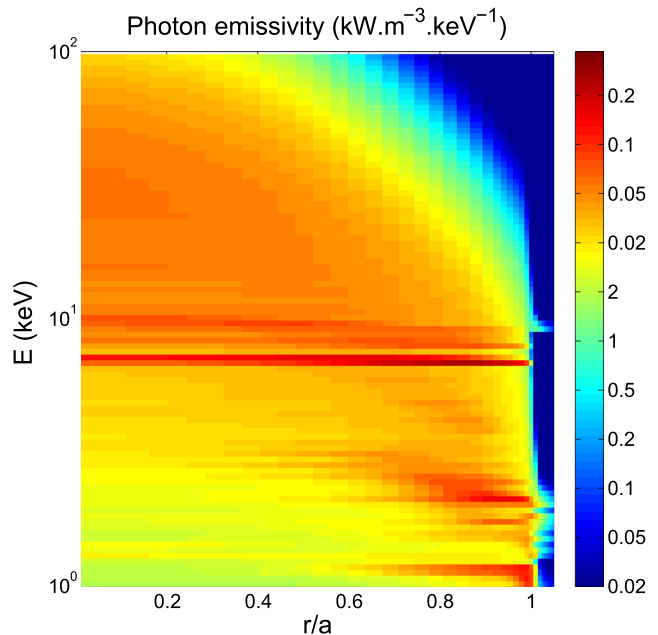


FIG. 5. Radiated power profile as a function of photon energy and normalized radius for the standard high power D-T scenario.⁵

density profile. The *adas810* database atomic data were used to estimate the line emission, and the SANCO impurity transport code was used to obtain a steady state equilibrium in predicted ITER plasma conditions. The resulting radiated profile is displayed in Fig. 5. The lines observed over the whole plasma around 7 keV are due to iron, and the 10 keV line results from tungsten line emission. Tungsten is also dominant in the plasma edge around 2 keV.

IV. SPECTRAL DECONVOLUTION

Energy deconvolution using the multi-anode LVIC is an ill-posed problem as we attempt to reconstruct a continuous spectrum from a finite number of measurements. Modeling of the solution is used to get rid of the ill-posedness of the problem. The shape of the incoming spectrum is modeled using a simple mathematical function, which depends on a limited number of parameters. This hypothesis can be made because the processes leading to x-ray emission in the plasma are well known (as long as good hypothesis are made on the plasma impurity content) and so is the expected emissivity spectrum. The mathematical function is defined in Sec. IV A. For any given parameters of the regularizing function, the currents that would be collected by each anode can be simulated. They will be labeled reconstructed currents, as opposed to the measured currents resulting from the synthetic diagnostic (which takes into account the full distributed incoming flux information). An algorithm is therefore used to find the parameters of the function, minimizing the difference between the measured and reconstructed currents. This algorithm is presented in Sec. IV B.

A. Hypothesis on the shape of the x-ray spectrum

As the processes leading to x-ray emission are well understood, the expected shape of the incoming spectrum is known. The low energy part of the spectrum (from 1 to 10 keV) is dominated by line emission (see Fig. 6). From around 15 keV, the x-ray photons result from continuous emission, which evolves as a decreasing exponential with energy.

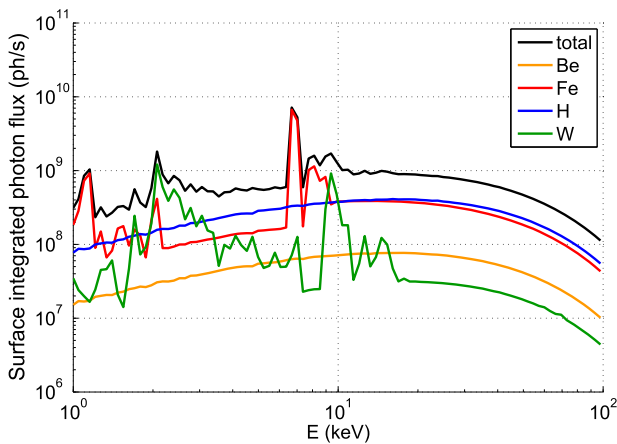


FIG. 6. Contribution of each impurity to the incoming photon flux of channel number 96. Channel number 96 corresponds to the radial line-of-sight, which goes through the very core of the plasma.

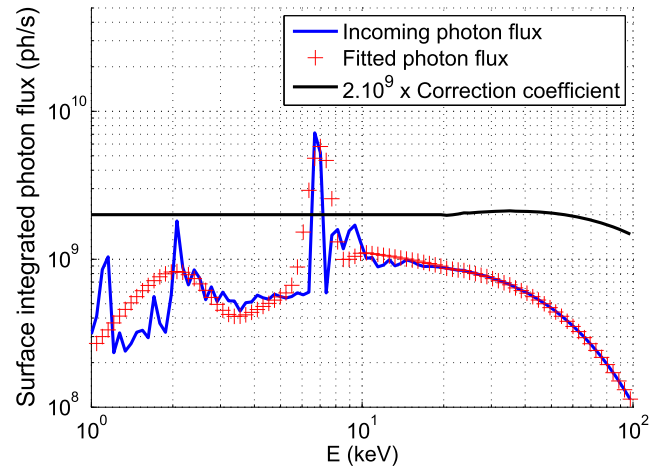


FIG. 7. Fitting of the channel number 96 incoming photon flux. Here, the parameters are $X_1 = 1.40 \cdot 10^9$ ph/s, $X_2 = 2.26 \cdot 10^{-2}$ keV $^{-1}$, $X_3 = 5.0 \cdot 10^9$ ph/s, and $X_4 = 6.0 \cdot 10^8$ ph/s.

A simple mathematical function based on four parameters has been used in order to fit the incoming (and well known) photon flux (see Fig. 7). Because bremsstrahlung emission results from several impurities and is integrated over a line with different electron temperatures, a decreasing exponential description is not completely accurate. In order to take into account these variations from the function, a correction coefficient C_{cor} is required. The “bremsstrahlung part” of the spectrum was chosen as the 10–100 keV range (it is the region in which bremsstrahlung is dominant) and is described by

$$f(h\nu > 10) = X_1 \cdot e^{-X_2 \cdot h\nu} \cdot C_{cor}(h\nu). \quad (5)$$

As the only available data come from this emissivity scenario, the actual correction coefficients for each line-of-sight C_{cor}^{LoS} have been computed and averaged in order to obtain a final coefficient, which has been used in this study: $C_{cor} = \frac{\sum_{i=1}^{n_{channel}} C_{cor}^{LoS}(i)}{n_{channel}}$. It is displayed in black in Fig. 7. The use of a single coefficient for all lines-of-sight, which integrate the plasma volume over very different electron temperatures, aims at demonstrating the robustness of this method with regard to geometry. A study of the impact of the electron temperature profile on the coefficient is required in order to validate this method for ITER operation, and this can be achieved by using different emissivity scenarios. It can be noticed that the coefficient is equal to 1 outside of the “bremsstrahlung part” of the spectrum.

The two remaining parameters of the function describe line emission peaks located at 2 and 7 keV,

$$f(h\nu < 10) = X_3 \cdot e^{-2 \cdot (h\nu - 7)^2} + X_4 \cdot e^{-1.5 \cdot (h\nu - 2)^2} + \frac{X_1 \cdot e^{-X_2 \cdot 10}}{10} \cdot h\nu. \quad (6)$$

The last part of the function is added in order to model a linear increase in the flux from 1 to 10 keV and ensure continuity at 10 keV. The width of each line emission peak has been chosen arbitrarily. The fitted peaks are wider than the actual peaks in

order to take into account additional radiation from neighboring peaks.

B. Minimization algorithm

Thanks to a hypothesis on the impurity content, we have established the shape of the incoming flux that we are trying to reconstruct. It is now necessary to compute the amplitude of the peaks and the coefficients (amplitude and slope) of the “bremsstrahlung part” of the spectrum: it is the set of coefficients that best fits the measured currents. An algorithm minimizing the difference between simulated and reconstructed measurements has been developed. The cost function of this method is defined as

$$r(X) = \sum (I^{\text{simu}} - I^{\text{rec}}(X))^2, \quad (7)$$

where $X = (X_1, X_2, X_3, X_4)$ is the vector of the function parameters, I^{simu} is the vector containing the measured currents simulated by the synthetic diagnostic tool, and I^{rec} is the vector containing the currents, which would be measured with an incoming photon flux $f(X)$.

The algorithm is based on the relaxation method. It works as follows:

- An initial X vector is computed. For the lines-of-sight looking at the very edge of the plasma (channel numbers 1, 192, and 193), this vector is taken as $X_{\text{ini}} = (10^9, 2 \cdot 10^{-2}, 5 \cdot 10^9, 10^9)$. The values of this initial vector have been chosen in order to be close to fitting the incoming spectrum while still needing significant modification from the algorithm. For other lines-of-sight, the initial X vector is taken as the resulting X vector of the previous line-of-sight in order to gain time by taking the space continuity of the emissivity into account. The scanning of lines-of-sight is performed from the plasma edge to plasma core (1–96, 192–97, and 193–252).
- For each X parameter, from X_1 to X_4 , a gradient descent with a constant step is performed until a minimal value of $r(X)$ is obtained. These gradient descents are repeated until the (X_1, X_2, X_3, X_4) vector stays the same from one iteration to the next.
- Several iterations of the last stage are performed with a decreasing step in order to fasten the reconstruction while keeping a high accuracy.

V. SINGLE LINES-OF-SIGHT RESULTS

The results of the previously described method and the fitness of each gas (argon and xenon) for energy deconvolution are discussed in this section. Quantification of the accuracy of reconstruction is also introduced.

A. Figure of merit

In order to assess the reconstruction accuracy, the following figure of merit is defined:

$$FOM_{\text{dec}} = \sqrt{\frac{\sum_{i=1}^{N_{\text{bins}}} dh\nu(i)^2 \cdot \left(\frac{\phi(i) - \phi^{\text{rec}}(i)}{\phi(i)}\right)^2}{\sum_{i=1}^{N_{\text{bins}}} dh\nu(i)^2}}, \quad (8)$$

where $dh\nu(i)$ is the width of the i -th energy band, N_{bins} is the amount of energy bins, ϕ is the photon flux impacting the detector, and ϕ^{rec} is the reconstructed photon flux.

Another figure of merit is used to depict how well the current is reproduced:

$$FOM_{\text{cur}} = \frac{1}{N_{\text{anodes}}} \sqrt{\sum_{i=1}^{N_{\text{anodes}}} \left(\frac{I^{\text{simu}}(i) - I^{\text{rec}}(i)}{I^{\text{simu}}(i)}\right)^2}. \quad (9)$$

In this work, we will consider that the function properly fits the incoming spectrum when FOM_{cur} is lower than 10^{-2} . This value came from a statistical analysis. Because the fitting function is very simple, it will not fit perfectly the incoming spectrum, which contains numerous peaks at low energy. Therefore, the obtained FOM_{dec} are quite high with regard to FOM_{cur} and will mostly be used to compare different reconstructions (e.g., with different gases).

B. Spectrum reconstruction using argon

For this study, a multi-anode LVIC with five anodes is simulated. In order to minimize the overlapping in the spectral response of each sub-chamber, it is necessary to use anodes of increasing length. The reconstruction is performed with argon under 5 bars of pressure, with anode sizes of 1, 3, 10, 35, and 100 mm and a 200 μm deep beryllium window. The dimensions of the anodes have been chosen in order to minimize the overlapping of the spectral responses of each sub-chamber and in order to maximize the accuracy of reconstruction. The resulting spectral responses are those displayed in Fig. 2.

The results of energy deconvolution using a multi-anode LVIC for channel number 96 (looking at the very core of the plasma) are displayed in the left panel of Fig. 8, and the figures of merit associated with this energy deconvolution are shown in the right panel of Fig. 8. It can be noted that the spectrum looks visually quite good. The high energy continuum ($h\nu \geq 10$ keV) is well reconstructed, with only a small difference between emissivity and reconstruction. The peak located around 8 keV is also well reconstructed in terms of integral: its amplitude is underestimated, but it is wider. The low energy peak is, however, clearly overestimated. The reconstruction of the low energy radiation is discussed in Sec. V D. The study of the figures of merit shows that good fitting of the currents is achieved for all the lines-of-sights except those located at the very edge of the plasma. This is explained by the fact that the spectrum of these lines-of-sight deviates too much from the model described by using Eqs. (5) and (6).

Inspection of an additional line-of-sight and the reconstruction of the line integrated x-ray emissivity in the given energy bands covering different parts of interest of the spectrum can be found in Ref. 10.

C. Spectrum reconstruction with xenon

A second set of reconstructions is performed with xenon at atmospheric pressure, with anode sizes of 5, 30, 60, 100, and 150 mm and a 200 μm deep beryllium window. The differences in size and pressure between argon and xenon are explained by the fact that we try to reproduce the shape with little overlapping in the spectral response while covering the whole energy range. The high pressure in the case of the argon detector comes from the fact that in order

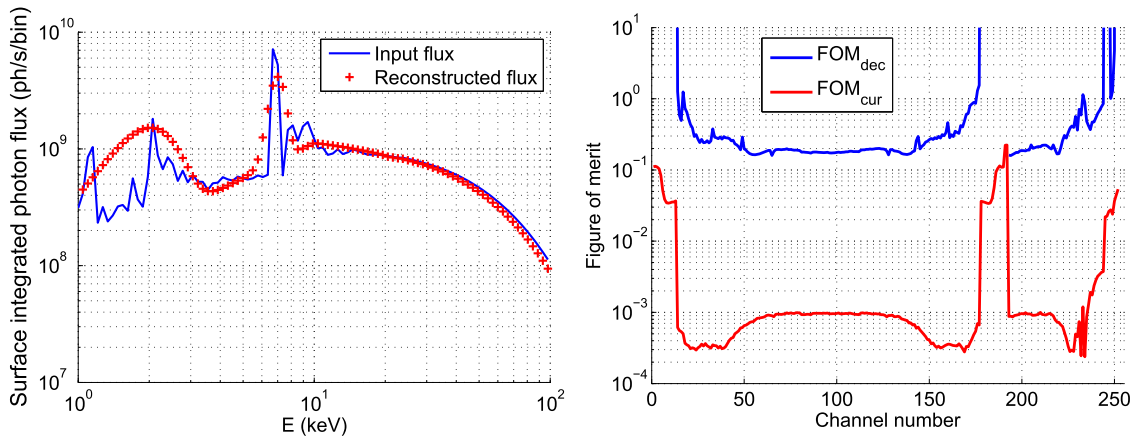


FIG. 8. Left: Energy deconvolution of the photon flux impinging channel number 96 (looking at the plasma core). Right: FOM_{dec} and FOM_{cur} of energy deconvolution. The multi-anode LVIC is filled with argon at five times the atmospheric pressure, with anode sizes of 1, 3, 10, 35, 60, and 100 mm and a 200 μm deep beryllium window.

to keep the detector of a size that could fit in the ITER port plug while retaining a high enough spectral response, argon requires a much higher pressure than xenon. The resulting spectral responses are displayed in Fig. 9. The peak in detection probability around 30 keV corresponds to the xenon $K - \alpha$ absorption edge, and the one at around 5 keV corresponds to its L absorption edge.²¹

The results of energy deconvolution with xenon at atmospheric pressure for channel number 96 (looking at the very core of the plasma) are displayed in Fig. 10. It can be noted that there is a very good agreement between incoming and reconstructed fluxes for $h\nu > 15$ keV. We can note that the W peak at 2 keV is not reconstructed [the coefficient X_4 from Eq. (6) is equal to 0]. The Fe peak at 7 keV is present, and its amplitude leads to an accurate integral of the peak. The continuum-dominated part of the spectrum is very well reconstructed: no significant difference can be observed.

The figures of merit for this energy deconvolution are displayed in the left panel of Fig. 11. It can be noted that the figures of merit

are of the same order of magnitude than the argon reconstruction and have a fairly similar shape.

The lines-of-sight exhibiting poor reconstruction are those aiming at the very edge of the plasma, where the emissivity does not match the hypothesis on the shape made in Sec. IV A. Indeed, it can be observed in the right panel of Fig. 11 that for a line-of-sight looking toward the plasma edge (channel number 10), the charge collected by sub-chambers 3–5 is not fitted by the algorithm. These sub-chambers mostly detect photons of energy higher than 10 keV (see Fig. 9), a range in which the emissivity at the very edge of the plasma does not follow the model of Eq. (5).

By comparing Figs. 8 and 10, we conclude that xenon is a better candidate than argon for energy resolved tomography due to its better accuracy at high energy. This conclusion is confirmed by the comparison of line integrated x-ray emissivity in the given energy bands for both gases.¹⁰

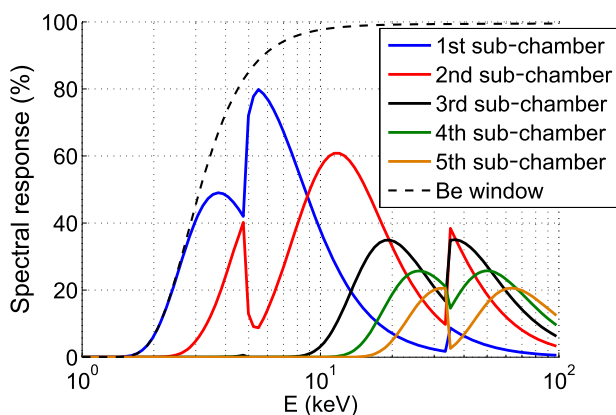


FIG. 9. Spectral response of each sub-chamber in the case of five anodes of the xenon LVIC at atmospheric pressure with anode sizes of 5, 30, 60, 100, and 150 mm and a 200 μm deep beryllium window.

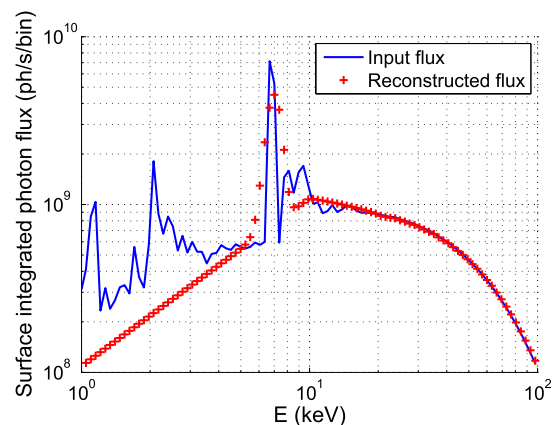


FIG. 10. Energy deconvolution of the photon flux impinging channel number 96 (looking at the plasma core). The multi-anode LVIC is filled with xenon at atmospheric pressure with anode sizes of 5, 30, 60, 100, and 150 mm and a 200 μm deep beryllium window.

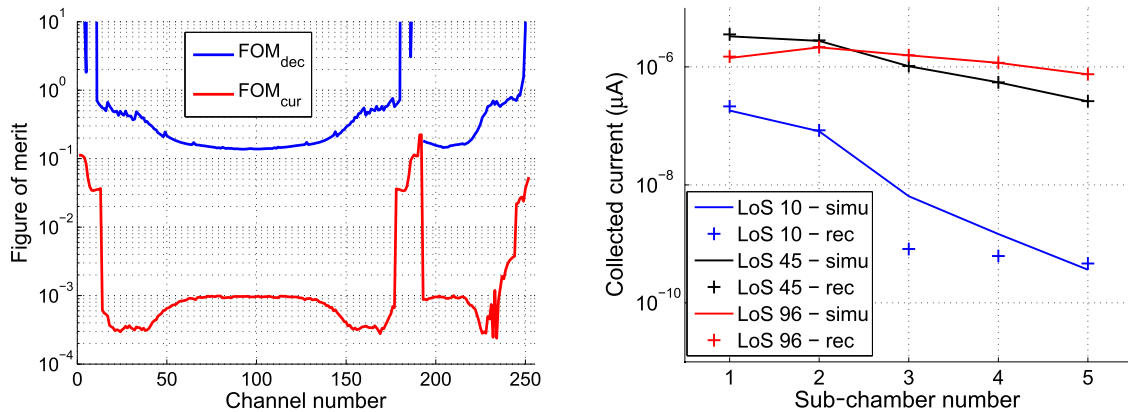


FIG. 11. Left: FOM_{dec} and FOM_{cur} of energy deconvolution technique. Right: Simulated and reconstructed currents for several lines-of-sight. The multi-anode LVIC is filled with xenon at atmospheric pressure with anode sizes of 5, 30, 60, 100, and 150 mm and a 200 μm deep beryllium window.

However, neither of these gases allows for an accurate reconstruction of the low energy part of the spectrum. The main hypothesis behind this error is the absorption through the beryllium window. We can, indeed, see in Fig. 9 that less than 40% of the flux is detected in the (2; 3) keV range.

D. Improving the reconstruction in the [2; 3] keV range

In order to verify the hypothesis formulated previously, a deconvolution has been performed with different beryllium window depths, with the parameters of the xenon simulation. As the beryllium window mostly absorbs photons of $h\nu < 5$ keV, the influence of the beryllium window is negligible outside of this energy range and therefore the reconstruction is not affected by its removal for $h\nu > 5$ keV. The reconstruction of the line integrated x-ray emissivity for each line-of-sight, integrated in between 2 and 3 keV, is displayed in Fig. 12.

With a 200 μm beryllium window, there is a clear overestimation (up to more than 100%) of the flux on the plasma edges and

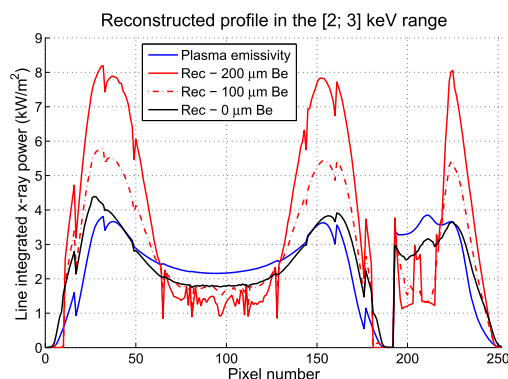


FIG. 12. Reconstruction of the line integrated x-ray emissivity in the [2; 3] keV range for each line-of-sight using xenon at atmospheric pressure with anode sizes of 5, 30, 60, and 100 and with different depths of the beryllium window.

underestimation (up to 50%) in the plasma core. Oscillations can be noticed in the core, which show that the reconstruction in this energy band is not stable.

A clear improvement of the reconstruction can be noted on the reconstructed flux as the beryllium window gets thinner. With a 100 μm beryllium window, the previously described reconstruction error is still present but with a much lower amplitude. The same can be said about the oscillations in the core. Without the beryllium window, there is still an underestimation in the core and overestimation in the edges, but their amplitude is much smaller than in the reconstruction with a beryllium window, and no oscillation is observed.

VI. ENERGY RESOLVED TOMOGRAPHY

In Sec. V, the incoming photon flux for each line-of-sight has been reconstructed. This photon flux is divided into 236 energy bins of increasing width. The method presented in this paper reconstructs the local x-ray emissivity by performing tomography for all the energy bins for which the energy is higher than 2 keV. The result of tomography is the reconstruction of the local emissivity at a given energy. By concatenating these local emissivities together, the energy resolved local emissivity is obtained.

For a given energy bin of energy $h\nu$, the deconvoluted photon flux profile is a fitting input for tomographic reconstruction. The photon flux in each bin must first be converted into the line integral of the emissivity through the line-of-sight for this particular energy bin,

$$f_{(meas)}(h\nu) = \frac{\phi(h\nu) \cdot h\nu}{E}, \quad (10)$$

where $f_{(meas)}$ is the line integral of the emissivity and E is the etendue of the aperture-detector system.

In this work, an algorithm based on the Tikhonov method,²² minimizing the Fisher information,²³ was used for energy resolved tomography. Anisotropic regularization limiting the gradients on the magnetic flux surfaces was applied in order to solve the inversion problem. This tomographic setup is the one used for soft x-ray tomography on the WEST tokamak.²⁴

A. Figures of merit

In order to assess the quality of tomographic reconstruction, four figures of merit are defined. First two figures of merit quantify the accuracy of tomographic reconstruction and are calculated over the region of the plasma core (defined as the region where $T_e > 10$ keV) and over the region enclosed by the last closed magnetic flux surface. They will be labeled FOM_{core} and FOM_{lcms} , respectively, and are given by

$$FOM = \frac{1}{N_P} \cdot \sqrt{\sum \frac{(\varepsilon_{(plasma)} - \varepsilon_{(rec)})^2}{\varepsilon_{(plasma)}^2}}, \quad (11)$$

where N_P is the number of geometrical pixels considered and $\varepsilon_{(plasma)}$ and $\varepsilon_{(rec)}$ are the plasma and reconstructed emissivities, respectively.

The third figure of merit is used to assess the fidelity of the fitting of the input line-of-sight profile by the algorithm. It is expressed as

$$FOM_{LoS} = \frac{1}{N_C} \cdot \sqrt{\sum (f_{(meas)} - f_{(rec)})^2}, \quad (12)$$

where N_C is the number of measurement channels and $f_{(meas)}$ and $f_{(rec)}$ are the measured and reconstructed line integrals of emissivity, respectively.

The last figure of merit is similar to FOM_{dec} from Eq. (8) but applied to the emissivity of each geometrical pixel in the tokamak. For a given pixel of coordinates (R, Z), the figure of merit is

$$FOM_{pix} = \sqrt{\frac{\sum_{i=1}^{N_{bins}} dh\nu(i) \cdot \left(\frac{\varepsilon(i) - \varepsilon_{rec}(i)}{\varepsilon(i)}\right)^2}{\sum_{i=1}^{N_{bins}} dh\nu(i)}}. \quad (13)$$

B. Results

The outputs (photon fluxes) from the xenon experiments of Sec. V have been used as inputs for tomography. Tomographic reconstructions have been performed independently for each energy

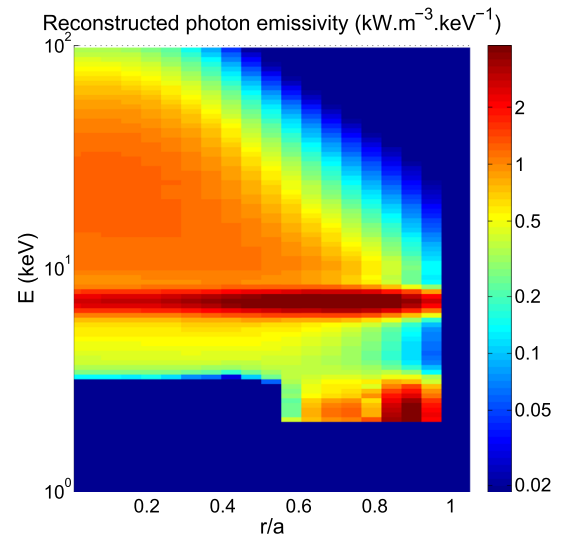


FIG. 13. Reconstructed radiated power profile as a function of photon energy and normalized radius with xenon at atmospheric pressure with anode sizes of 5, 30, 60, 100, and 150 mm and a 200 μm deep beryllium window.

bin from 2 to 100 keV. Below 2 keV, the spectral response of the LVIC does not allow for a good enough current measurement (most of the photons are stopped in the beryllium window), and therefore, these energy bands are not considered.

The results of this energy resolved tomography can be visualized through the reconstructed radiated profile in Fig. 13. Visual differences can be observed with the input radiated profile (Fig. 5). However, the overall shape and value are similar for both profiles. The W lines around 2 keV at the plasma edge and the Fe line at 7 keV are qualitatively reconstructed. This is a good result as this method could allow for an estimation of the W concentration in the plasma edge.

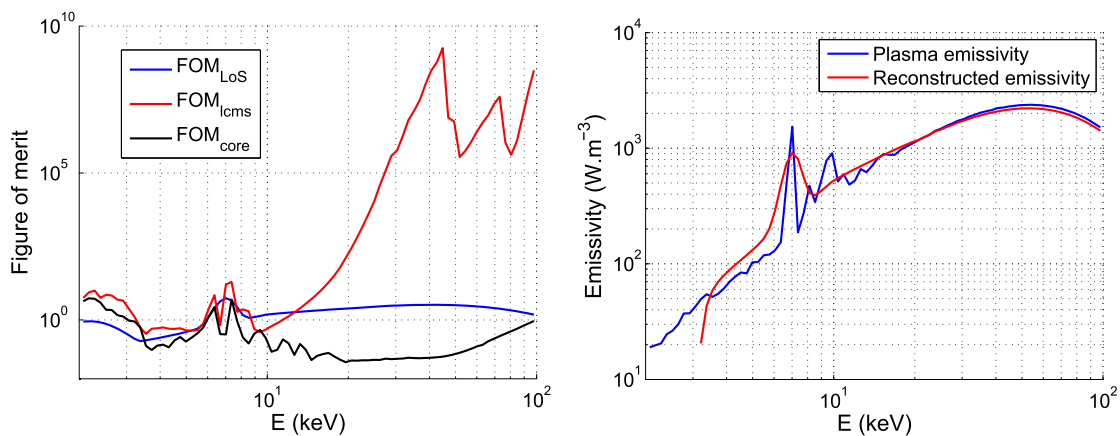


FIG. 14. Left: Figures of merit of energy resolved tomography: FOM_{LoS} , FOM_{lcms} , and FOM_{core} . Right: Reconstruction of the local plasma emissivity in the plasma core (at $R = 6.27$ m and $Z = 0.57$ m). For this pixel, $FOM_{pix} = 3.7 \cdot 10^{-3}$. The multi-anode LVIC is filled with xenon at atmospheric pressure with anode sizes of 5, 30, 60, 100, and 150 mm and a 200 μm deep beryllium window.

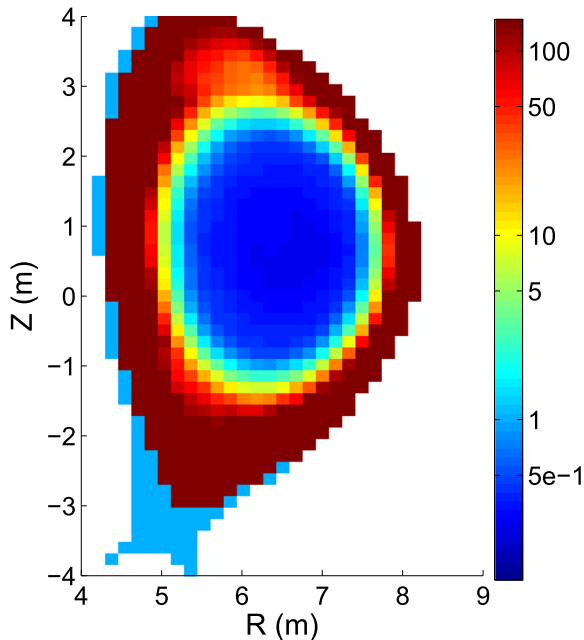


FIG. 15. Figure of merit FOM_{pix} of energy resolved tomography. The multi-anode LVIC is filled with xenon at atmospheric pressure with anode sizes of 5, 30, 60, 100, and 150 mm and a 200 μm deep beryllium window.

A more quantitative estimation of the accuracy of reconstruction is provided by an analysis of the figures of merit. FOM_{Los} , FOM_{lcms} , and FOM_{core} are displayed in Fig. 14.

For each energy bin, the backfitting of the line integrated emissivity is fairly stable with energy with an increase around 7 keV. This shows that the tomographic algorithm has struggled to reconstruct the profiles corresponding to the second peak of the spectrum model, but overall, the discrepancy in the input data was well spread over all the energy bins. FOM_{lcms} and FOM_{core} quantify the accuracy of the reconstruction of the x-ray emissivity in the whole plasma and in the core. It can be observed that for the line emission part of the spectrum ($h\nu < 15$ keV), the emissivity is well reconstructed with both figures of merit around 1. In the “bremsstrahlung part” of the spectrum ($h\nu > 15$ keV), the core exhibits a very good reconstruction with FOM_{core} around 10^{-1} . However, when we look at the whole plasma, we can observe a very high loss of accuracy with energy: FOM_{lcms} goes up to almost 10^{10} . This is explained by the facts that the plasma edge does not emit much at high energies and that the tomographic algorithm tends to be less accurate in the edges.

The reconstruction of the local emissivity for a pixel located at the very core of the plasma ($R = 6.27$ m, $Z = 0.57$ m) is displayed in the right panel of Fig. 14. We can observe that the agreement between the shape of the local emissivity and its reconstruction is quite good. This is confirmed by the low FOM_{pix} value obtained for this pixel.

FOM_{pix} is shown in Fig. 15. This figure of merit quantifies the difference between the local emissivity and its reconstruction. Similarly as with FOM_{lcms} and FOM_{core} , it can be observed that the plasma core exhibits a much higher reconstruction accuracy with $FOM_{pix} < 10^{-2}$.

VII. ESTIMATION OF THE ELECTRON TEMPERATURE

At high energy, the plasma emissivity is proportional to $\exp\left(-\frac{h\nu}{kT_e}\right) = \exp\left(-\frac{h\nu}{2\pi k T_e}\right)$.²⁵ Therefore, an exponential fitting of the local reconstructed emissivity can allow for an estimation of the local electron temperature, and thus, doing this for each pixel leads to electron temperature profiles. This has been performed using the energy resolved local plasma emissivity presented in Sec. VI B. The original electron temperature profile is displayed in the left panel of Fig. 16.

Similarly as for tomography, a figure of merit quantifying the accuracy of reconstruction is used in the scope of this study. It can be estimated over the plasma core or over the whole region enclosed by the last closed magnetic surface. It is given by

$$FOM = \frac{1}{N_p} \cdot \sqrt{\sum \frac{(T_e^{(input)} - T_e^{(rec)})^2}{(T_e^{(input)})^2}}. \quad (14)$$

The result of the reconstruction of the electron temperature is shown in the right panel of Fig. 16. The corresponding FOM_{lcms} and FOM_{core} are 0.55 and 0.35, respectively. Compared to the previous reconstructions, these values are quite high, but it can be observed that the visual aspect of the electron temperature (shape and amplitude) is well reproduced. The analysis of the relative error (see Fig. 17) confirms the good accuracy of the reconstruction at the very core of the plasma. A ring of $\approx 40\%$ of error surrounds that region, making this result valid only where the electron temperature is the highest. An improvement of this result could be achieved by an increase in the amount of sub-chambers or by the use of a different method, which could potentially perform spectral deconvolution and tomography simultaneously, as described in Ref. 26. In a plasma with a higher temperature, this method should be valid in a wider region.

VIII. SENSITIVITY ANALYSIS

In this section, the influence of perturbation on the measurement is investigated. A statistical analysis is performed on the energy deconvolution method, considering 100 reconstructions with a Gaussian noise with a 1% amplitude. The results of a tomographic reconstruction and the related electron temperature computation in the same noise configuration are also presented.

A. Energy deconvolution

In order to estimate the performance of the method under perturbative noise, a sensitivity analysis has been performed. A random noise following a Gaussian distribution with an amplitude of 1% has been added to the currents measured in the case of a xenon LVIC at atmospheric pressure with anode sizes of 5, 30, 60, 100, and 150 mm and a 200 μm deep beryllium window. In order to gather enough statistics for estimating the stability of the method with regard to noise, the impact of noise has been recorded in 100 simulations. The highest and lowest reconstructions are used to create the so-called envelope, inside which a 1% noise reconstruction is most likely to be located.

FOM_{dec} and its envelope, as well as the line integrated x-ray emissivity in the continuum-dominated energy range, are displayed

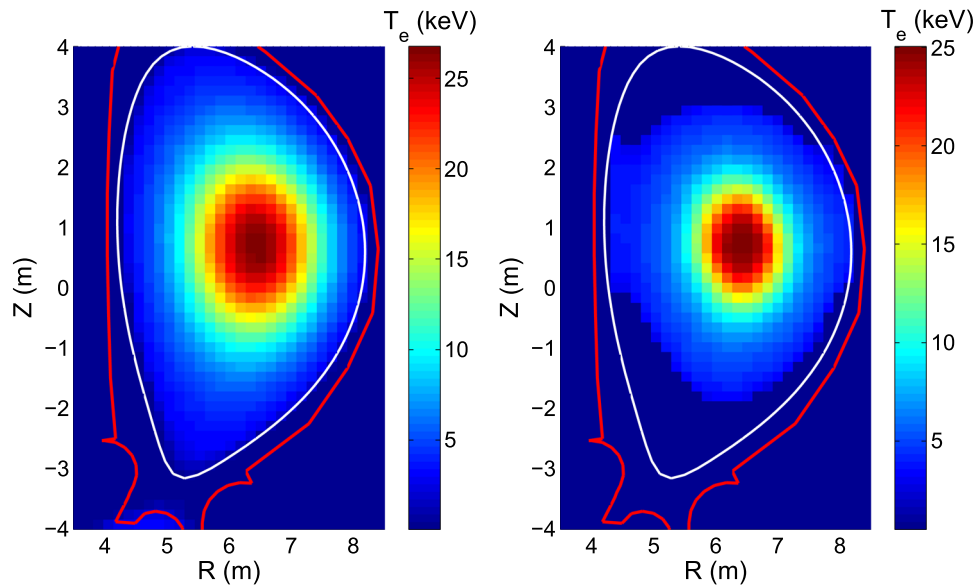


FIG. 16. Left: Electron temperature profile of the ITER standard high power D–T scenario. Right: Reconstructed electron temperature profile obtained after energy resolved tomography. Xenon LVICs with anodes sizes of 5, 30, 60, 100, and 150 mm and a beryllium window of $200\ \mu\text{m}$ were used in this case.

in Fig. 18. In terms of figure of merit, the noise does not necessarily have a great impact, and in some cases, the figure of merit is actually lowered by the presence of noise. The “continuum part” of the spectrum exhibits a high resilience to noise with a maximal error of around 10%. The high energy end of the spectrum has the highest impact on FOM_{dec} from Eq. (8) because $dh\nu$ increases exponentially

with energy. Therefore, it is possible that instabilities occur at low energy as these energy ranges do not have a high weight on the FOM_{dec} 1% noise envelope. A more complete study of the impact of noise can be found in Ref. 10 and can be summarized as follows: the low energy part of the spectrum exhibits high instabilities with up to ten times overestimation of the emissivity and the (6, 10) keV range is more stable, but a significant underestimation (of around 30%) can be obtained.

The impact of noise on energy discrimination is quite high under 10 keV, where the spectrum is dominated by emissivity peaks. However, the “bremsstrahlung part” of the spectrum and its exponential decrease are much more stable to such perturbations.

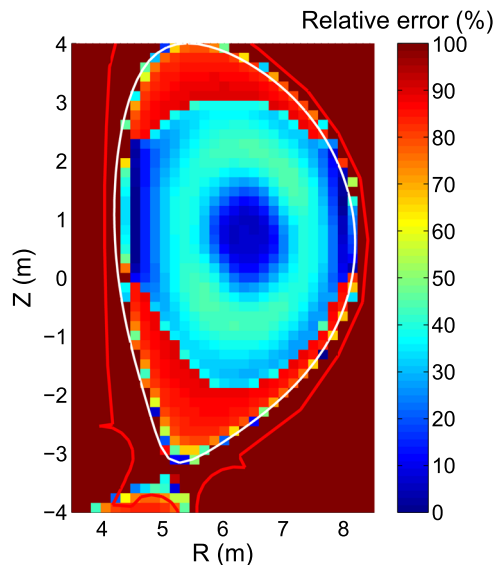


FIG. 17. Relative error of the electron temperature reconstruction. The multi-anode LVIC is filled with xenon at atmospheric pressure with anode sizes of 5, 30, 60, 100, and 150 mm and a $200\ \mu\text{m}$ deep beryllium window.

B. Energy resolved tomography

The results of an energy deconvolution simulation with a Gaussian perturbative noise of 1% on the measurement have been used as inputs for tomography, as described in Sec. VI.

The reconstruction of local emissivity in the plasma core is displayed in the left panel of Fig. 19. The high energy end of the spectrum is quite accurate; however, in the [2; 10] keV region, the reconstruction is inaccurate (especially below 4 keV). The peak at around 2 keV is, indeed, extremely overestimated, and the peak at 7 keV is better, although clearly overestimated as well. In this range, the sensitivity to perturbation is quite high, which corroborates the envelopes obtained in Figs. 18 and 19. The use of a different method or the addition of smoothing on the inputs for tomography might improve the reconstruction at low energy. Due to the error levels obtained in the low energy part of Fig. 19 (there is up to a factor 10^4 between plasma emissivity and its reconstruction), the spectrum has been divided into two energy bands {[4; 10] and [10; 100] keV} for the calculation of the FOM_{pix} figure of merit, which is displayed in

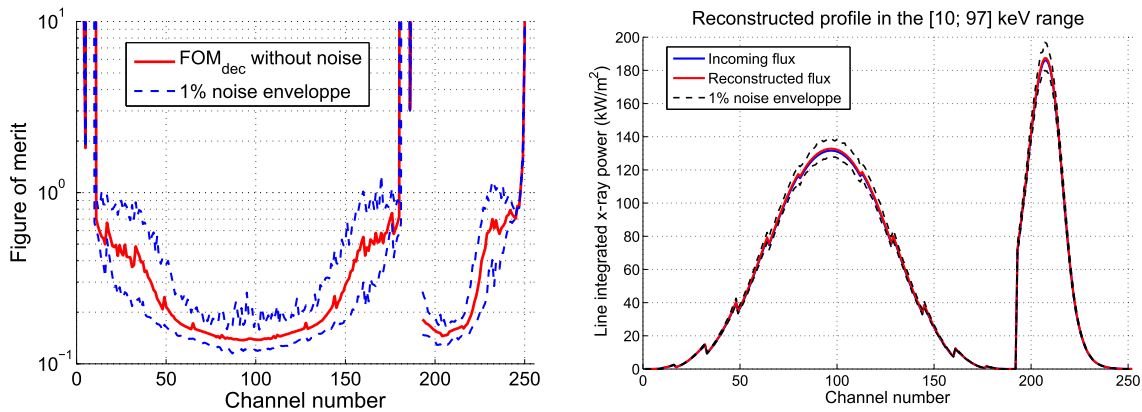


FIG. 18. Left: FOM_{dec} and its 1% noise envelope of energy deconvolution technique. Right: Reconstruction of the line integrated x-ray emissivity in the [10; 97] keV range and its 1% noise envelope for each line-of-sight. The multi-anode LVIC is filled with xenon at atmospheric pressure with anode sizes of 5, 30, 60, 100, and 150 mm and a $200\ \mu\text{m}$ deep beryllium window.

Fig. 20. FOM_{pix} exhibits a high value in the [4; 10] keV range in the whole plasma, but higher accuracy is observed in the plasma core. This shows that, even though the second peak is not very well reconstructed by energy resolved tomography, its accuracy is higher in the plasma core. We can observe that FOM_{pix} displays a low and constant value over the whole plasma core in the [10; 100] keV range, which indicates a satisfactory spectral deconvolution in this region and energy range. It is worth mentioning that in the scope of computing the electron temperature from the local emissivity spectrum, only the high energy range is of interest. Therefore, the addition of noise to this method should not prohibit the reconstruction of the electron temperature profile.

The other figures of merit used to assess the quality of tomography are shown in the right panel of **Fig. 19**. Overall, it can be noted that the figures of merit are of the same order of magnitude as those of **Fig. 14**, without perturbative noise. The shape of FOM_{core} and FOM_{lcms} has not changed much with the addition of noise, at the

exception of the low energy part (from 2 to 4 keV) where these figures of merit increase by several orders of magnitude because of the addition of noise. For photon energies higher than 4 keV, no significant difference can be observed in FOM_{core} due to the addition of perturbation. This means that the reconstruction of the plasma core is very resilient to perturbative noise. The value of FOM_{lcms} is much higher at high energies where it can reach up to 10^{15} compared to 10^{10} without noise. This is explained by the fact that the plasma edge does not emit much high energy photons, and therefore, a small perturbation can lead to a big relative overestimation of the emissivity.

The study of FOM_{LoS} shows that the addition of noise does not affect much the ability of the tomographic algorithm to fit the input data. It can be concluded that the addition of noise for energy resolved tomography leads to high relative error at high energy on the plasma edge. However, the plasma core exhibits a very good reconstruction in this energy range.

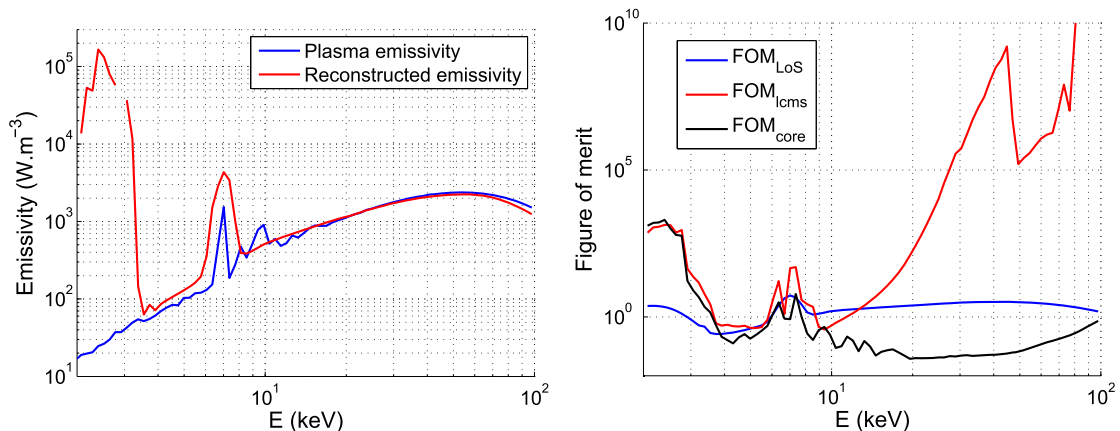


FIG. 19. Left: Reconstruction of the local emissivity in the plasma core (at $R = 6.27\ \text{m}$ and $Z = 0.57\ \text{m}$) with 1% of perturbative noise added to the measurement. Right: Figures of merit of energy resolved tomography: FOM_{LoS} , FOM_{lcms} , and FOM_{core} , with 1% of Gaussian perturbative noise on the LVIC measurement. The multi-anode LVIC is filled with xenon at atmospheric pressure with anode sizes of 5, 30, 60, 100, and 150 mm and a $200\ \mu\text{m}$ deep beryllium window.

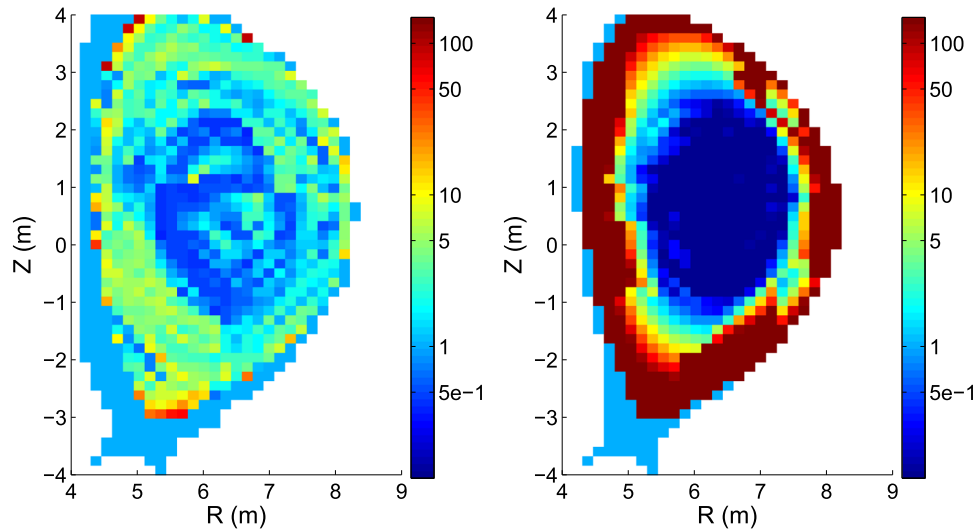


FIG. 20. Left: Figure of merit FOM_{pix} of energy resolved tomography with 1% of Gaussian perturbative noise on the LVIC measurement computed in [4; 10] keV range. Right: Figure of merit FOM_{pix} of energy resolved tomography with 1% of Gaussian perturbative noise on the LVIC measurement computed in the [10; 100] keV range. The multi-anode LVIC is filled with xenon at atmospheric pressure with anode sizes of 5, 30, 60, 100, and 150 mm and a 200 μm deep beryllium window.

C. Electron temperature profile

The electron temperature has been computed from the local emissivity spectra obtained in Sec. VIII B, following the method described in Sec. VII, and is shown in the left panel of Fig. 21. The overall shape and intensity of the profile are satisfactory, although

it seems more blurry than in the reconstruction without perturbation. The relative error, displayed in the right panel of Fig. 21, shows that the electron temperature in the core is quite accurate, but this accuracy has suffered from the addition of noise. There has been an increase in the reconstruction error in the blue ring; the error is now around 50% instead of 40. Overall, it can be concluded that the

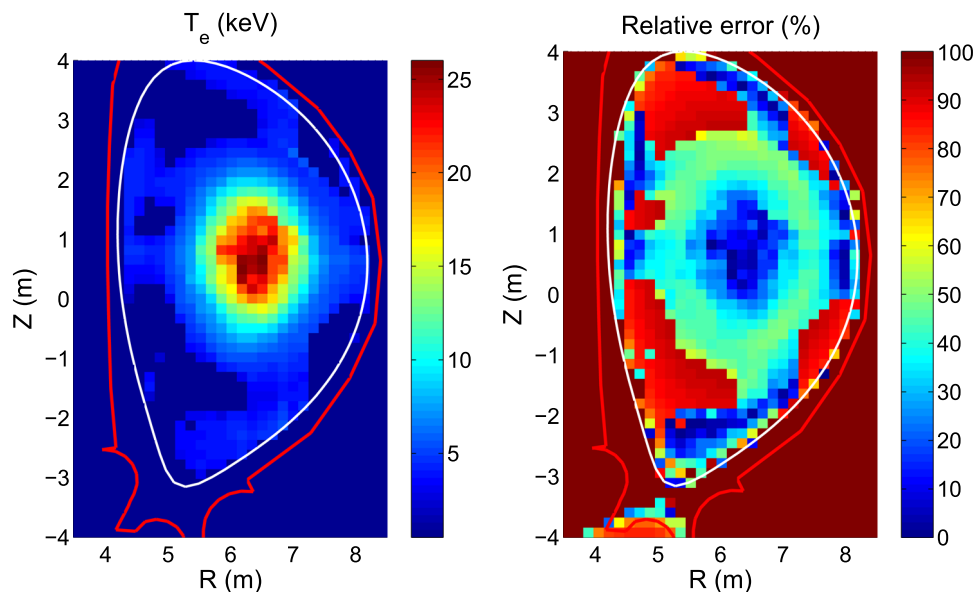


FIG. 21. Left: Reconstructed electron temperature profile obtained after energy resolved tomography with 1% of Gaussian perturbative noise on the LVIC measurement. Right: Relative error of the electron temperature reconstruction with 1% of Gaussian perturbative noise on the LVIC measurement. Xenon LVICs with anodes sizes of 5, 30, 60, 100, and 150 mm and a beryllium window of 200 μm were used in this case.

electron temperature reconstruction seems to be quite resilient to this perturbation.

IX. CONCLUSION

For SXR measurements, traditional semiconductors cannot be considered for ITER due to their low resilience to fast particles and the LVIC seems to be an adequate solution. Through this work, we have proposed a new way to make use of multi-anode LVICs, which shows an interesting capability to perform energy resolved x-ray measurement on ITER. An original deconvolution method to obtain a continuous spectrum from a finite amount of measurement has been developed and tested through modeling. The influence of the LVIC filling gas has been studied through the comparison of argon and xenon, under different pressure conditions, which concluded that xenon is the best candidate of the two for performing an accurate reconstruction of the spectrum in a rather broad energy range. However, the reconstruction of the low energy part of the spectrum displays a very low resilience to such perturbations. Reconstructed line integrated emissivity has been used as inputs for tomography in order to obtain spectrally resolved radiation power profiles. Good accuracy has been observed in the comparison of the reconstructed profiles to the original ones. Fitting of the high energy range of the local emissivity spectrum has been performed in order to reconstruct the electron temperature profile from x-ray measurement. The accuracy of the electron temperature profile is satisfying at the very core of the plasma. This is not a surprise; indeed, emissivity is rather low at the edge and accuracy of the reconstructed impinging spectrum at the same location is less accurate. The sensitivity of the energy deconvolution method to perturbative noise has been investigated as well, concluding that the method is viable for 1% noise levels in the high energy range ($h\nu > 10$ keV). Energy resolved tomography has been performed with such a noise level, showing that the accuracy is quite good at high energy but not satisfactory below 10 keV. Reconstruction of the electron temperature proved to be fairly resilient to this perturbation, especially in the plasma core.

The LVIC with multiple anodes and the proposed associated method of deconvolution seems to be very promising for ITER, which presents very high core temperature. In these conditions and setup, information on spectral distribution and electron temperature profiles can be obtained from discrete measurements.

ACKNOWLEDGMENTS

The authors would like to thank Christian Ingesson for his extremely valuable inputs. They would like to thank their Chinese colleagues from ASIPP for their fruitful inputs, especially regarding the input geometry for the Diagnostic First Wall (DFW) apertures and in-plug slits. This work was supported by the ITER Organization through Grant No. SSA72. The views and opinions expressed in this paper do not necessarily reflect those of the ITER Organization nor those of Fusion for Energy.

This work was carried out within the framework of the EUROfusion Consortium and received funding from the Euratom research and training program 2014–2018 and 2019–2020 under Grant Agreement No. 633053. The views and opinions

expressed herein do not necessarily reflect those of the European Commission.

DATA AVAILABILITY

The data that support the findings of this study are available from the corresponding author upon reasonable request.

REFERENCES

- W. J. Nuttall, Intitute of physics report, fusion as an energy source: Challenges and opportunities, https://www.iop.org/publications/iop/2008/file_38224.pdf, 2008.
- V. Philipps, R. Neu, J. Rapp, U. Samm, M. Tokar, T. Tanabe, and M. Rubel, "Comparison of tokamak behaviour with tungsten and low-Z plasma facing materials," *Plasma Phys. Controlled Fusion* **42**, B293 (2000).
- R. Neu, K. B. Fournier, D. Schlögl, and J. Rice, "Observations of x-ray spectra from highly charged tungsten ions in tokamak plasmas," *J. Phys. B: At., Mol. Opt. Phys.* **30**, 5057 (1997).
- A. Jardin, D. Mazon, P. Malard, M. O'Mullane, M. Chernyshova, T. Czarski, K. Malinowski, G. Kasprovicz, A. Wojenski, and K. Pozniak, "On a gas electron multiplier based synthetic diagnostic for soft x-ray tomography on WEST with focus on impurity transport studies," *J. Instrum.* **12**, C08013 (2017).
- M. O'Mullane, "Energy resolved radiated power simulations for ITER bolometer study," ITER Internal Report No. ITER_D_Q4L9G8, 2015.
- R. Reichle, "SRD-55 (Diagnostics) from DOORS," ITER Internal Report No. ITER_D_28B39L, 2020.
- L. Hu, K. Chen, Y. Chen, H. Cao, S. Li, H. Yu, J. Zhan, J. Shen, S. Qin, X. Sheng *et al.*, "Preliminary design and R&D of ITER diagnostic-radial X-ray camera," *Nucl. Instrum. Methods Phys. Res., Sect. A* **870**(Supplement C), 50–54 (2017).
- D. Mazon, M. Chernyshova, G. Jiolat, T. Czarski, P. Malard, E. Kowalska-Strzeczwick, S. Jablonski, W. Figacz, R. Zagorski, M. Kubkowska *et al.*, "Design of soft-X-ray tomographic system in WEST using GEM detectors," *Fusion Eng. Des.* **96–97**, 856–860 (2015).
- D. Vezinet, D. Mazon, and P. Malard, Capteur de rayonnement électromagnétique et/ou de particules. Brevet 1356278, déposé le 28 juin 2013
- D. Colette, *Innovative X-Ray Diagnostic for Impurity Transport on ITER* (Aix-Marseille Université, 2021).
- D. Colette, D. Mazon, R. Barnsley, A. Sirinelli, A. Jardin, M. O'Mullane, and M. Walsh, "Modeling a low voltage ionization chamber based tomography system on ITER," *Rev. Sci. Instrum.* **91**, 073504 (2020).
- L. C. Ingesson, P. J. Böcker, R. Reichle, M. Romanelli, and P. Smeulders, "Projection-space methods to take into account finite beam-width effects in two-dimensional tomography algorithms," *J. Opt. Soc. Am. A* **16**, 17–27 (1999).
- M. J. Berger, J. H. Hubbell, S. M. Seltzer, J. Chang, J. S. Coursey, R. Sukumar, D. S. Zucker, and K. Olsen, "XCOM: Photon cross sections database," NIST Standard Reference Database 8, 87-3597, 2009.
- T. Watanabe, H. W. Schnopper, and F. N. Cirillo, "K x-ray fluorescence yield of argon," *Phys. Rev.* **127**, 2055–2057 (1962).
- M. Hribar, A. Kodre, and J. Pahor, "The determination of the K-shell fluorescence yield of xenon by use of the proportional counter method," *Z. Phys.* **280**, 227 (1977).
- U. Fano, "Ionization yield of radiations. II. The fluctuations of the number of ions," *Phys. Rev.* **72**, 26–29 (1947).
- L. G. Christophorou, V. E. Anderson, and J. B. Birks, *Atomic and Molecular Radiation Physics* (Wiley-Interscience, New York, 1971).
- H. Sakurai and B. D. Ramsey, "Dependence of energy resolution on anode diameter in xenon proportional counters," *Nucl. Instrum. Methods Phys. Res., Sect. A* **313**(1–2), 155–160 (1992).
- A. Hashiba, K. Masuda, T. Doke, T. Takahashi, and Y. Fujita, "Fano factor in gaseous argon measured by the proportional scintillation method," *Nucl. Instrum. Methods Phys. Res., Sect. A* **227**(2), 305–310 (1984).

- ²⁰N. Ishida, J. Kikuchi, T. Doke, and M. Kase, "Fano factor in xenon," *Phys. Rev. A* **46**(3), 1676 (1992).
- ²¹T. H. V. T. Dias, J. M. F. dos Santos, P. J. B. M. Rachinhas, F. P. Santos, C. A. N. Conde, and A. D. Stauffer, "Full-energy absorption of x-ray energies near the Xe L- and K-photoionization thresholds in xenon gas detectors: Simulation and experimental results," *J. Appl. Phys.* **82**, 2742 (1997).
- ²²A. N. Tikhonov, A. V. Goncharsky, V. V. Stepanov, and A. G. Yagola, *Numerical Methods for the Solution of Ill-Posed Problems* (Springer Science & Business Media, 2013), Vol. 328.
- ²³A. Jardin, D. Mazon, and J. Bielecki, "Comparison of two regularization methods for soft x-ray tomography at Tore Supra," *Phys. Scr.* **91**, 044007 (2016).
- ²⁴D. Mazon, D. Vezinet, D. Pacella, D. Moreau, L. Gabelieri, A. Romano, P. Malard, J. Mlynar, R. Masset, and P. Lotte, "Soft x-ray tomography for real-time applications: Present status at Tore Supra and possible future developments," *Rev. Sci. Instrum.* **83**, 063505 (2012).
- ²⁵G. H. McCall, "Calculation of X-ray bremsstrahlung and characteristic line emission produced by a Maxwellian electron distribution," *J. Phys. D: Appl. Phys.* **15**, 823 (1982).
- ²⁶J. Mlynar, T. Craciunescu, D. R. Ferreira, P. Carvalho, O. Ficker, O. Grover, M. Imrisek, J. Svoboda, and JET Contributors, "Current research into applications of tomography for fusion diagnostics," *J. Fusion Energy* **38**, 458–466 (2019).